RSC Advances

PAPER

View Article Online
View Journal | View Issue

Cite this: *RSC Adv.*, 2017, **7**, 36697

Two-step ball-milling synthesis of a Si/SiO_x/C composite electrode for lithium ion batteries with excellent long-term cycling stability†

Lingzhi Qian,[a] Jin-Le Lan,[*ab] Mengyao Xue,[a] Yunhua Yu*[a] and Xiaoping Yang[a]

SiO_x-based anodes have attracted tremendous attention owing to their low cost, higher theoretical capacity than graphite and lower volume expansion than pure silicon. In this work, a simple and cost-effective two-step ball-milling method was proposed to fabricate Si/SiO_x/C composites by using commercial SiO and graphite carbon as raw materials. The two-step ball-milling synthesis of the Si/SiO_x/C composites can avoid the generation of an inert SiC phase and realize the uniform dispersion of Si/SiO_x in graphite carbon, which offers good electrical conductivity and relieves the volume expansion of the Si/SiO_x phase. Owing to the synergistic effect of the Si/SiO_x phase and the graphite carbon, the typical Si/SiO_x/C electrode exhibits a stable and high capacity of 726 mA h g^{-1} after 500 cycles at a current density of 0.1 A g^{-1} with a capacity retention of 82%. The two-step ball-milling preparation of the Si/SiO_x/C composite provides a facile approach to fabricate high-performance SiO_x-based anode materials.

Received 15th June 2017
Accepted 20th July 2017

DOI: 10.1039/c7ra06671f

rsc.li/rsc-advances

1. Introduction

With the rapid increase of environmental problems and people's growing demands, lithium-ion batteries (LIBs) have attracted a great deal of attention and been widely used in electric vehicles and portable electronics due to their inherent advantages such as high energy density, long cycle life and non-memory effect.[1–3] However, the commercial graphite anode material of LIBs, which offers a specific capacity of only 372 mA h g^{-1} and limited power density,[4] cannot meet the increasing demand for high-energy storage capacity. Therefore, novel anode materials with high specific capacity and high power density are highly desirable.

Silicon is an attractive anode material for LIBs due to the highest theoretical capacity of 4200 mA h g^{-1}.[5,6] However, the huge volume change during the charge and discharge process can cause a pulverization of the electrode and electric disconnection from current collectors, resulting in poor cycling stability. To tackle this problem, a variety of carbon frameworks such as 0D hollow carbon spheres,[7] 1D CNFs[8] and 2D graphene[9] were utilized to support Si nanoparticles. Nevertheless, owing to the difficulty in dispersion and the high cost of pure nano-silicon material, many scientists have paid attention to other inexpensive Si-based alternative materials such as silicon monoxide (SiO), which has obvious advantages of relatively smaller volume change.[10] In recent years, there have been many reports on the fabrication of SiO/C composites as anode materials in LIBs by a simple high-energy ball-milling (HEBM) process.[11–15] For instance, Chil-Hoon Doh's group[14] prepared a SiO/C anode through a simple one-step high-energy ball milling process, which showed a reversible charge capacity value of 688 mA h g^{-1} at the 30th cycle with 99% coulombic efficiency. Later, W. Y. Yoon's group[15] used a W coating to improve the conductivity of one-step ball-milled SiO–graphite composite, exhibiting better charge and discharge behavior under higher current. However, it was found that one-step ball milling for the mixture of SiO and graphite could create an electrochemical inactive phase of SiC,[16] reducing the specific capacity of the composites. Therefore, it is a challenge to avoid the formation of SiC phase in the fabrication of SiO/C composites by HEBM process.

In this work, a simple two-step HEBM method was used to prepare Si/SiO_x/C composites by using SiO and graphite powders as raw materials. The as-obtained Si/SiO_x/C electrode exhibited a stable and high reversible capacity (726 mA h g^{-1} at a rate of 100 mA g^{-1} after 500 cycles) due to the uniform coating of graphite on the surface of Si/SiO_x particles and avoiding the formation of inert component SiC by the two-step ball-milling process.

2. Experimental

2.1. Synthesis of Si/SiO_x/C composites

The precursors used for this synthesis were SiO (Aladdin, −200 mesh) and commercial graphite (Aladdin, −200 mesh) powders.

[a]State Key Laboratory of Organic-Inorganic Composites, Beijing University of Chemical Technology, Beijing 100029, China. E-mail: yuyh@mail.buct.edu.cn; lanjl@mail.buct.edu.cn; Fax: +86-10-6442-2084; Tel: +86-10-6442-7698

[b]Changzhou Institute of Advanced Materials, Beijing University of Chemical Technology, Beijing 100029, China

† Electronic supplementary information (ESI) available. See DOI: 10.1039/c7ra06671f

All chemical reagents were used directly without further purification. The Si/SiO_x/C composites were prepared through the high-energy mechanical ball-milling (HEBM) method. Typically, 5 g SiO powder was placed in a 300 ml stainless steel vessel containing stainless steel balls by a planetary mill (QM-1 SP04, Nanjing University Instrument Plant, China) with a rotation speed of 400 rpm. Two kinds of the stainless steel ball with diameters of 6 and 10 mm was used, and the number ratio was 2 : 1. The weight ratio of the stainless steel ball to the SiO powder was 30 : 1, and the vessel was filled with argon gas. The SiO in the vessel were milled for different times (2, 6, 10 and 12 h) at 400 rpm. Then, the resultant Si/SiO_x particles (~4 g) were mixed with graphite powders at different weight ratio (5 : 1, 5 : 2 and 5 : 3), and subjected to HEBM for 40 min under the same balling conditions, respectively, to obtain Si/SiO_x/C composites. Correspondingly, the as-prepared Si/SiO_x/C samples were denoted as Si/SiO_x/C-1, Si/SiO_x/C-2 and Si/SiO_x/C-3, respectively. For comparison, Si/SiO_x/C-3 composite was fabricated by using one-step balling–milling method under the same balling conditions for 10 h.

2.2. Sample characterization

The morphologies and EDS mapping of the powder samples were analyzed by a field emission scanning electron microscope (FE-SEM, Supra55, Carl Zeiss) and a high resolution transmission electron microscope (HR-TEM, Tecnai G_2 F_{30} S-TWIN). The phase structure of the samples was investigated by using a wide-angle X-ray diffractometer (XRD, WAXD, D_8 Advance, Bruker, Cu Kα, λ = 0.154 nm) and a Raman spectrometer (Renishaw, INVIA). An X-ray photoelectron spectrometer (XPS, EscaLab 250, Thermo Fisher Scientific) was used to analyze the elemental chemical status of samples. Thermogravimetric analysis was carried out on a TGA instrument (TA-Q50, America) at a heating rate of 10 °C min^{-1} from 40 to 800 °C in air to measure the amounts of components.

2.3. Electrochemical measurements

The Si/SiO_x/C composite was mixed with carbon black and poly(vinylidene difluoride) (PVDF) to form a slurry at a weight ratio of 8 : 1 : 1 in *N*-methyl pyrrolidone (NMP). The working electrode was prepared by casting the slurry onto nickel foil through a doctor blade method, and then dried in a vacuum oven at 120 °C for 24 h. The cells were assembled in an Ar-filled glovebox by using a Li metal foil as the counter electrode and the Celgard 2300 membrane as a separator. The electrolyte was 1 M LiPF6 in ethylene carbonate (EC)/dimethyl carbonate (DMC) (1 : 1 v/v). After assembly, cyclic voltammetry (CV) measurements were performed between 0.005 and 3 V by using an Autolab PGSTAT 302 N (Metrohm) workstation with a scan rate of 0.1 mV s^{-1}. The galvanostatic charge/discharge measurements were carried out between 0.005 and 3.0 V on a Land CT2001A (China). Electrochemical impedance spectroscopy (EIS) measurements were also carried out at the same electrochemical workstation with the amplitude of 10 mV and a frequency ranging from 10 kHz to 0.1 Hz. The mass loading of the active materials (~1.0 mg cm^{-2}), including both Si/SiO_x and C, was taken into account when the capacities were calculated.

3. Results and discussion

Fig. 1 illustrates the fabrication process of Si/SiO_x/C composite. Firstly, the SiO powder was ball-milled and underwent a disproportionation reaction into micro–nano Si/SiO_x particles,[17–20] which possessed abundant electrochemical active sites for lithium storage. Then the second step ball-milling process was performed on the mixtures of the Si/SiO_x particles and graphite with different weight ratios for a short time to produce Si/SiO_x/C composites.

Fig. 2(a) shows the XRD patterns for commercial Si, SiO and graphite(C) and the as-prepared Si/SiO_x, and Si/SiO_x/C-3 composites. For the commercial Si (Aladdin, 30 nm), the typical peaks at 28.3°, 47.2°, and 56.1° correspond to the (111), (220), (331) lattice orientations of Si. Comparing to the XRD pattern for the SiO sample, a slight increase of the Si peak (28.3°) height and a slight decrease of the SiO_2 peak (22° and 26.4°) height were detected in the XRD pattern of the as-prepared Si/SiO_x sample, indicating the slight effect of HEBM process on the phase structure of SiO. For the Si/SiO_x/C-3 composite, a slight increase was seen in the C peak (26.4°), which overlapped with the peak (26.4°) of SiO_2 in the pattern of Si/SiO_x sample. The peak at 43.4° and 44.5° corresponds to the Fe_2Si (PDF#83-1259), which is the possible production of the Si and the stainless steel ball during HEBM. As shown in Fig. 2(b), the Si/SiO_x/C-3 sample fabricated by the one-step ball-milling method showed the typical peak of SiC phase at 35.6°, however, which didn't appear in the XRD pattern of the Si/SiO_x/C-3 sample obtained by two-step ball-milling method. In order to further clarify the presence of SiC phase, the XRD patterns of pure SiC and Si/SiO_x/C-3 composite fabricated by one-step ball milling were conducted as shown in Fig. S2.† We can observed the typical peak at 35.6° corresponding to the pure SiC that clearly show the presence of SiC. The absence of the SiC phase in the two-step ball-milling synthesized Si/SiO_x/C-3 sample is favor for enhancing the electrochemical performance of Si/SiO_x/C electrode.

The surface morphologies and microstructures of Si/SiO_x and Si/SiO_x/C samples were investigated by using SEM and HRTEM. As shown in Fig. 3(a) and (b), the Si/SiO_x (10 h) and Si/SiO_x/C-3 composite showed similar particle morphologies. Fig. 3(c)–(f) show the corresponding EDS mapping for Si, O and

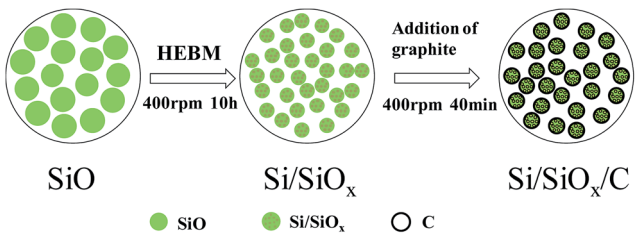

Fig. 1 Schematic diagram of the two-step ball-milling fabrication process of Si/SiO_x/C composite.

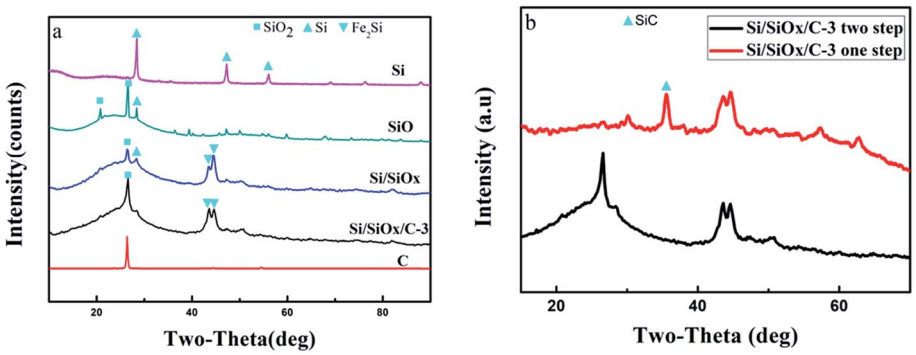

Fig. 2 XRD patterns of (a) Si, SiO, Si/SiO_x (HEBM 10 h), graphite(C), and Si/SiO_x/C-3 composite and (b) Si/SiO_x/C-3 composite fabricated by one-step ball-milling and two-step ball-milling.

C of the Si/SiO_x/C composites, which reveals a homogeneous distribution of Si, O and C in the composite. In the Si/SiO_x/C-3 composite, graphitic carbon with a weight percent of ~25 wt% (Fig. S1†) provided a good electrical conductivity and an effective buffering matrix that improve the cycle performance. As shown in Fig. 3(g), some nanosized crystallites with size ranging from 3 to 10 nm were finely dispersed within the crystallized graphite phase and homogeneously encapsulated by it. In Fig. 3(h), the lattice fringes show an interplanar spacing of about 0.312 nm, which corresponds to Si (111) planes.[21,22] In Fig. 3(i), the lattice fringes show an interplanar spacing of 0.212 nm, corresponding to SiO_2 (311) planes.[23,24] The most of lattice fringes in Fig. 3(i) except the marked SiO_2 (311) planes, which are corresponded to the crystallized graphite. The detailed valence distribution of silicon elements can be obtained from XPS analysis.

The XPS spectra of the Si/SiO_x/C-3 composites are shown in Fig. 4. The full spectra of Si/SiO_x/C-3 in Fig. 4(a) further confirm the presence of O, C, and Si elements. Fig. 4(b) shows the high-resolution XPS spectra of Si 2p, which can be fitted into five peaks, corresponding to five different Si oxidation states: Si^0(98.7 eV), Si^+(101.1 eV), Si^{2+}(102.2 eV), Si^{3+}(103.5 eV) and Si^{4+}(104.6 eV).[25,26] The XPS results of Si 2p confirms the presence of Si and SiO_x in the Si/SiO_x/C composite. Three peaks at

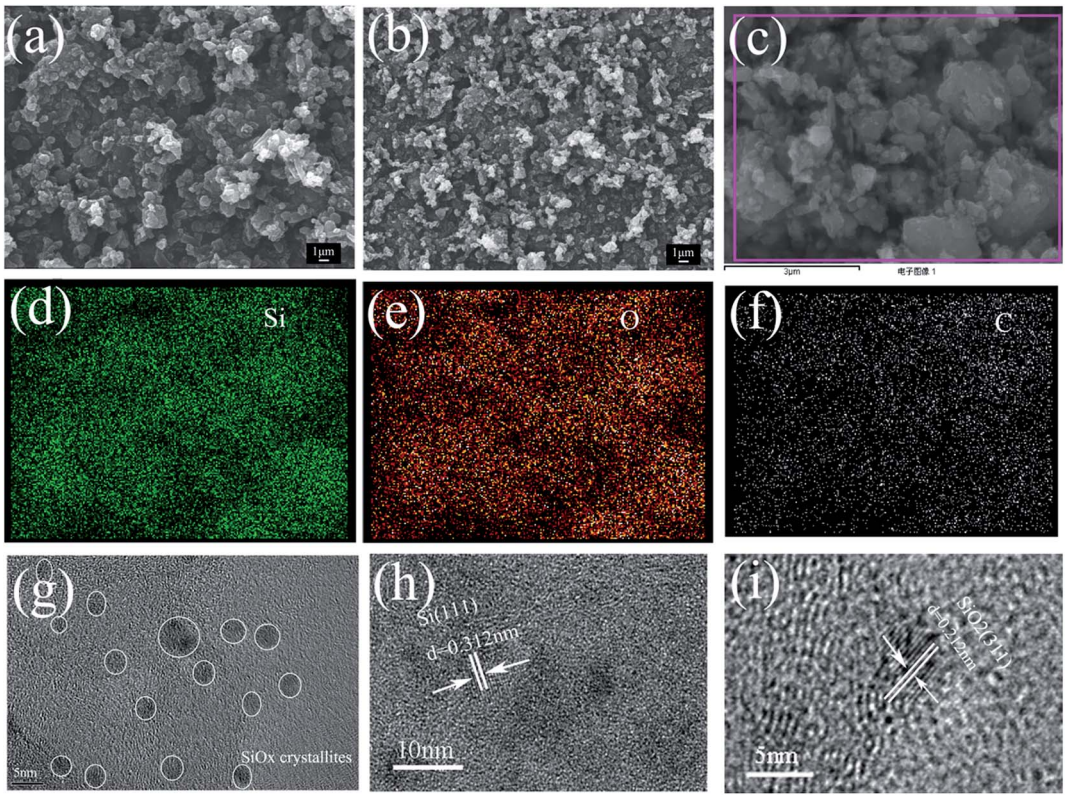

Fig. 3 SEM images of the ball-milled (a) Si/SiO_x 10 h, (b) Si/SiO_x/C-3, (c)–(f) corresponding EDS mapping images of silicon, oxygen and carbon. (g–i) HRTEM images of Si/SiO_x/C-3 composite.

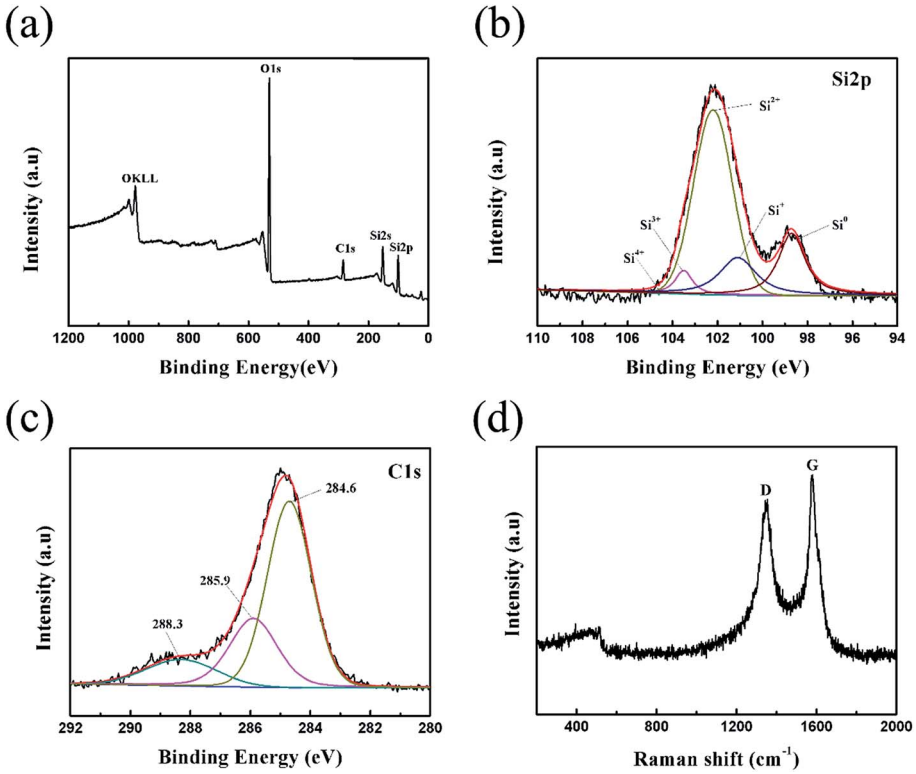

Fig. 4 XPS spectra (a) full spectra, (b) Si 2p spectra, (c) C 1s spectra and (d) Raman spectra of Si/SiO_x/C-3 composite.

284.6 eV, 285.9 eV and 288.3 eV were founded in Fig. 4(c) by fitting the C 1s spectrum, which may be assigned to C–C bonds in the free carbon matrix, C–O bonds and C=O bonds, respectively. No peaks at less than 284.6 eV were observed, suggesting that the absence of C–Si bonds.[27] Fig. 4(d) presents the Raman spectrum of Si/SiO_x/C-3 sample. It displays a broad peak at around 491 cm^{-1}, which is ascribed to the Si/SiO_x nanoparticles, in which nanosilicon uniformly exists in SiO_x particles.[28,29] What is more, the two characteristic Raman peaks at 1348 cm^{-1} and 1576 cm^{-1} are observed, which are the D-band for the disordered mode and the G-band for the stretching mode of C–C bonds of graphite.[30,31] Generally, the intensity ratio of D band to G band (I_D/I_G) is used to estimate the degree of disorder in graphite.[32] The I_D/I_G ratio for the Si/SiO_x/C-3 sample is 0.855, suggesting that the graphite in the sample has high graphitization degree, which is favor for improving the electrochemical performance of Si/SiO_x/C composites.

In order to get an optimal ball-milling time, the electrochemical properties of a series of Si/SiO_x samples ball-milled for different times (up to 12 h) were investigated as anode materials for LIBs. As shown in Fig. 5(a), the specific capacities of the Si/SiO_x series were declined quickly in the first few cycles. Among them, the Si/SiO_x sample ball-milled for 10 h showed a little bit better performance than the other samples, so it was chosen as the raw material in the subsequent fabrication of Si/SiO_x/C composites. Fig. 5(b) shows the cycling stability at room temperature of the Si/SiO_x/C series with different weight ratios of Si/SiO_x (10 h) to graphite (5 : 1, 5 : 2 and 5 : 3), corresponding to the graphite contents in the samples are about 10, 15 and 25%, respectively, as shown in Fig. S1.† Clearly, the Si/SiO_x/C series presented far better cycle performance than the Si/SiO_x (10 h). Moreover, the cycling performance of Si/SiO_x/C was improved along with the increase of graphite content. However, the first charge capacities and discharge capacities decreased as increasing graphite content. The reason is that the content of active mass of Si/SiO_x is least in the Si/SiO_x/C-3, which cause the lower initial capacity. However, the carbon cannot completely relieve the volume expansion of Si/SiO_x in Si/SiO_x/C-1 and Si/SiO_x/C-2, which cause the worse cycling performance. Finally, considering the comprehensive performance in terms of good cycling stability, high capacity and initial coulombic efficiency, the Si/SiO_x/C-3 composite was considered the optimal sample for further investigation in this work.

In Fig. 5(c), the Si/SiO_x (10 h) electrode delivered the first charge and discharge capacities of 1021.4 and 406.7 mA h g^{-1} with an initial coulombic efficiency of about 39.8%, showing no commercial value. The Si/SiO_x electrode exhibited a similar potential profile to those of reported SiO and SiO_x electrodes in the first lithium insertion and extraction.[33,34] Generally, the high irreversible capacity could be explained by the formation of nanosilicon and Li_2O. Then, the nanosilicon reacts with Li to form Li–Si alloy.[35] An obvious difference exists between the first discharge voltage profile and the subsequent ones. As shown in Fig. 5(d), the Si/SiO_x/C-3 electrode exhibited the first discharge capacity of 881.4 mA h g^{-1} and a charge capacity of 649 mA h g^{-1}, with an initial coulombic efficiency of about 73.6%, which improved a lot compared to the Si/SiO_x electrode (39.8%). In the second cycle, the coulombic efficiency increased to 94.3%. The

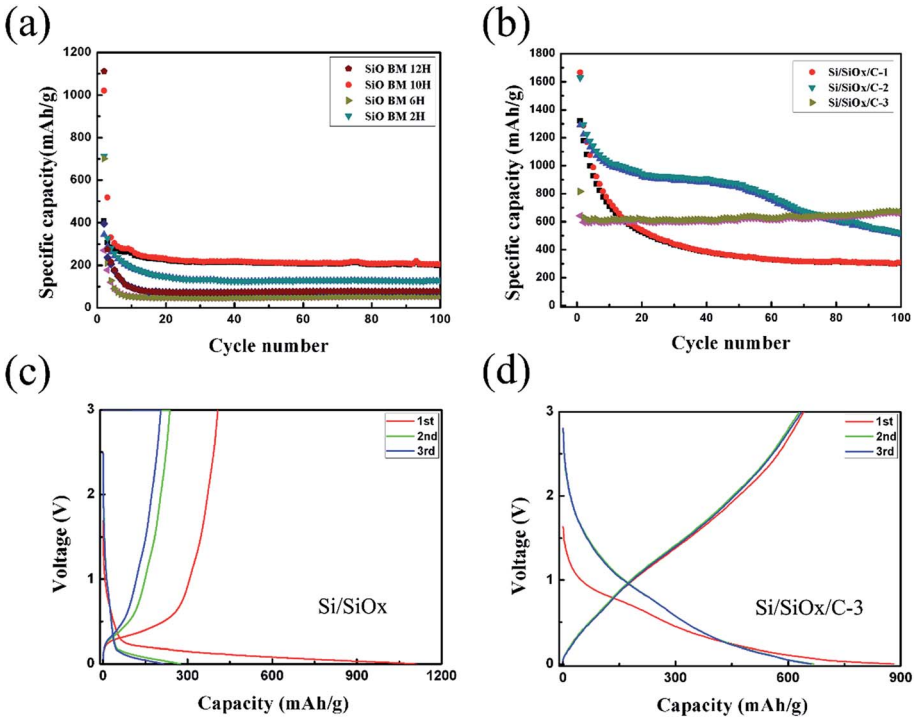

Fig. 5 Cycle performances of (a) Si/SiO_x ball-milled for different times and (b) the Si/SiO_x/C series with different weight ratios of Si/SiO_x (10 h) to graphite, charge and discharge voltage profiles of (c) Si/SiO_x (10 h) and (d) Si/SiO_x/C-3 samples at a current density of 0.1 A g^{-1}.

first cycle seemed different from the others due to the formation of SEI film. In the subsequent lithiation process, a negative potential overshoot is observed due to the nucleation of new phases such as Li_2O and lithium silicates.[36] The carbon layer effectively prevents the electrode crushing caused by volume expansion of Si/SiO_x. If the electrode crushed, Si/SiO_x electrode will continue to contact with the electrolyte and form the SEI film repeatedly. Therefore, the carbon layer contributes to form a stable SEI film. Comparing with the charge and discharge voltage profiles of Si/SiO_x/C-1 and Si/SiO_x/C-2 in Fig. S4,† we find the redox potential of Si/SiO_x/C is similar, which could not consider corresponding to the redox potential of neither Si nor graphite. The unexpected performance may be ascribed to the complexity and synergistic effect of the ball-milled nanocomposites.

The two-step ball-milling fabricated Si/SiO_x/C-3 electrode displayed stable cycle performance and maintained a reversible charge capacity and discharge capacity of 732 and 726 mA h g^{-1} after 500 cycles at a current density of 0.1 A g^{-1}, as shown in Fig. 6(a). The first charge/discharge capacity of Si/SiO_x/C-3 (one-step) electrode were about 408.8 and 325 mA h g^{-1}, significantly lower than those of the Si/SiO_x/C-3 (two-step) electrode (881.4 and 649 mA h g^{-1}). This can be explained by the fact that the inert SiC phase is formed in the one-step ball milling process, which reduces the capacity of Si/SiO_x/C-3 electrode. Compared to SiO and Si/SiO_x electrodes, the two-step ball-milling fabricated Si/SiO_x/C-3 electrode shows excellent long-term cycle performance. The capacity decay of Si/SiO_x/C composite is almost negligible, indicating its good cycle stability. Fig. 6(b) presented the charge and discharge capacity at different current densities of 0.1, 0.2, 0.5, 1 and 0.1 A g^{-1} and the corresponding reversible capacity was 650.9, 561.6, 483.3, 412.4 and 693.8 mA h g^{-1}, respectively. When the current density gradually increased from 0.1 to 1 A g^{-1}, the electrode presented a stable discharge capacity at each current density. When the current density was switched back to 0.1 A g^{-1}, the capacity can be recovered almost completely to the original value, indicating the stable structure of the electrode. Fig. 6(c) shows the cyclic voltammetry curves of the Si/SiO_x/C composite electrodes at a scanning rate of 0.1 mV s^{-1} between 0 and 3 V for the first three cycles. In the first cycle, there are two reduction peaks at about 1.46 and 0.34 V, both of which disappear from the second cycle. The peak at 1.46 V is associated with the electrolyte decomposition and the formation of the solid electrolyte interface (SEI) layer.[37] The broad peak at 0.34 V corresponds to the reduction reactions of SiO_x, while the broad anodic peaks at 0.38 and 0.52 V correspond to the dealloying process of Li_xSi and a part of $Li_2Si_2O_5$,[38,39] attributing to the delithiation of Li_xSi back to amorphous Si.[40] In the subsequent cycles, a new cathodic peak appears at about 0.21 V and becomes more intense with the activation of the electrode in third cycle, corresponding to the lithiation of amorphous silicon.[23] The electrochemical impedance spectroscopy (EIS) technique was also utilized to clarify the electrochemical performance of the Si/SiO_x/C composites compared with Si/SiO_x materials. The horizontal axis of EIS spectra represents the high to low frequency range. As shown in Fig. 6(d), the first semicircle at the high-to-medium frequency range corresponds to the impedance of the SEI film (Ω_1); the second semicircle at the medium-to-low frequency range corresponds to the impedance of the Li-ion transfer across the

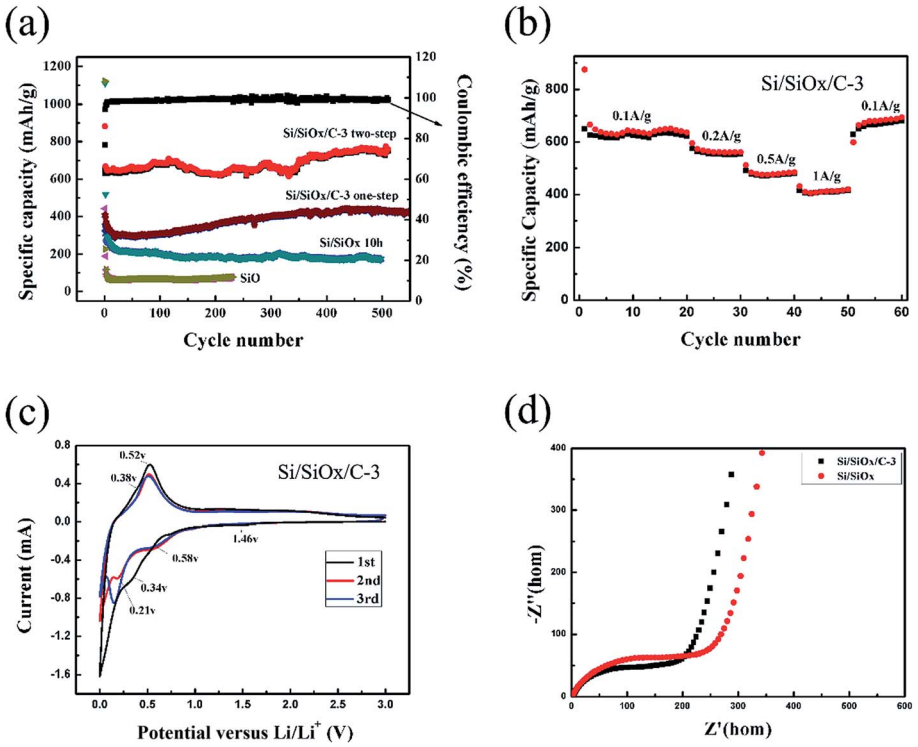

Fig. 6 (a) Cycle performance and coulombic efficiency at a current density of 0.1 A g^{-1}, (b) rate performance at different rates and (c) the first three CV curves at a scan rate of 0.1 mV s^{-1} between 0 and 3 V for Si/SiO_x/C-3 electrode, and (d) EIS results for Si/SiO_x and Si/SiO_x/C-3 electrode.

interface between the SEI film and the electrode (Ω_2); and the inclined line at the low frequency range is ascribed to the impedance of Li-ion diffusion in the bulk electrode (Ω_3).[41,42] With the Si/SiO_x/C-3 composite, both Ω_1 and Ω_2 have been reduced, suggesting that Si/SiO_x/C-3 composite can facilitate the formation of a stable, dense SEI film[43,44] and improve Li-ion transfer rate.[45,46]

Fig. 7 summarizes the contribution of each component in the Si/SiO_x/C-3 sample. According to the TG analysis (Fig. S1†), the weight content of carbon in Si/SiO_x/C-3 composite is about 25%. Calculating the capacity of Si/SiO_x/C-3 composite according to the formula (Si/SiO_x effect × 75% + C effect × 25%). The capacity of C, which is evaluated as the same condition by ball-milling 40 min as shown in Fig. S3.† It displayed a reversible charge capacity and discharge capacity of 135.4 and 135.2 mA h g^{-1} after 500 cycles at a current density of 0.1 A g^{-1}. Compared with the calculated specific capacity (1st, 840 mA h g^{-1}; 500th, 162 mA h g^{-1}), the Si/SiO_x/C-3 electrode exhibits higher specific capacity (1st, 881 mA h g^{-1}; 500th, 726 mA h g^{-1}), indicating a great synergistic effect between Si/SiO_x and graphite carbon. The presence of graphite carbon stabilizes the Si/SiO_x particles during cycling process to accommodate more lithium ions and

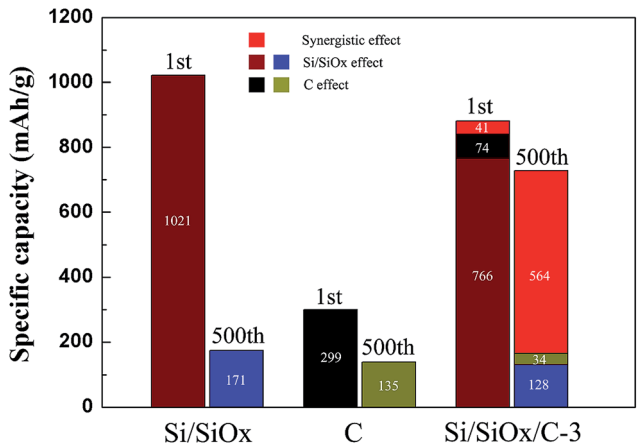

Fig. 7 The 1st and 500th reversible charge specific capacities of Si/SiO_x, C and Si/SiO_x/C-3 electrode, and the calculated specific capacity based on experimental values.

Table 1 Comparison of electrochemical properties of SiO_x-based anodes

Structure	Charge capacity (mAh g^{-1})	Current density (mA g^{-1})	Cycle number	Coulombic efficiency first time (%)	Ref.
SiO/C	688	100	30	44.5	14
SiO/CNFs	700	100	200	35.7	11
Nano-sized SiO_x	660	100	50	44	48
SiO_x–C	674.8	100	100	77	49
SiO_x@C nanorods	720	100	350	69	22
Si–$NiSi_2$–Al_2O_3@C	580	100	200	76.8	21
This work	726	100	500	73.6	

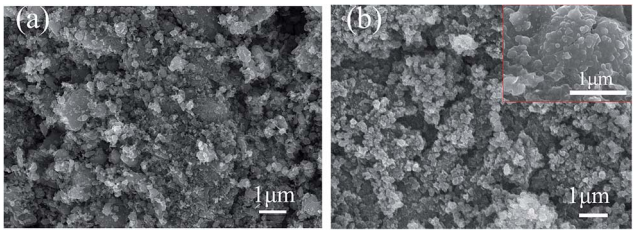

Fig. 8 SEM images of the Si/SiO_x/C-3 composites electrode (a) before cycling and (b) after 500 cycles.

keeps the active materials electrically interconnected.[47] Therefore, the Si/SiO_x/C electrode exhibits significantly enhanced capacity and cyclability. Nearly 70% capacity of Si/SiO_x/C-3 after 500 cycles is ascribed to the synergistic effect. Further, it can be seen from Table 1 that the Si/SiO_x/C-3 electrode showed the cycle performance better than many other reported SiO_x-based electrodes.

Fig. 8 shows the morphological and structural change of the Si/SiO_x/C-3 electrode before and after cycling. As shown in Fig. 8(b), the SEI layer was observed on the electrode surface after 500 cycles, and no cracking or pulverization of the electrode caused by the volume change was observed, suggesting that the structural integrity of the Si/SiO_x/C-3 electrode was maintained well during cycling. Therefore, the Si/SiO_x/C-3 electrode showed a long-term cycle performance.

4. Conclusions

In summary, Si/SiO_x/C composites were fabricated by using a simple and cost-effective two-step ball-milling process with the commercial SiO and graphite carbon as raw materials. Comparison with the one-step ball-milling process of SiO/C, the two-step ball-milling process can avoid the generation of inert SiC phase in the fabrication of Si/SiO_x/C electrodes, providing more electrochemical active sites. Meanwhile, graphitic carbon coated on the surface of Si/SiO_x uniformly and relieved its volume expansion. Owing to the synergistic effect of Si/SiO_x and graphite carbon, the typical Si/SiO_x/C composite used as an anode for LIBs shows high specific capacity, excellent long-term cycle performance, giving a superior reversible capacity of 726 mA h g^{-1} at a rate of 0.1 A g^{-1} after 500 cycles. The two-step ball-milling preparation of Si/SiO_x/C composite provides a facile approach for fabricate high-performance silicon-based anode materials.

Acknowledgements

This work was financially supported by National Natural Science Foundation of China (No. 51272021, 51142004 and 51402010) and Natural Science Foundation of Jiangsu Province (BK20140270).

References

1 J. Maier, *Nat. Mater.*, 2005, **4**, 805–815.
2 M. Armand and J. Tarascon, *Nature*, 2008, **451**, 652–657.
3 A. S. Arico, P. Bruce, B. Scrosati, J. M. Tarascon and W. V. Schalkwijk, *Nat. Mater.*, 2005, **4**, 366–377.
4 N. A. Kaskhedikar and J. Maier, *Adv. Mater.*, 2009, **21**, 2664–2680.
5 H. C. Shin, J. A. Corno, J. L. Gole and M. Liu, *J. Power Sources*, 2005, **139**, 314–320.
6 J. Yin, M. Wada, K. Yamamoto, Y. Kitano, S. Tanase and T. Sakai, *J. Electrochem. Soc.*, 2006, **153**, A472–A477.
7 N. Liu, H. Wu, M. T. McDowell, Y. Yao, C. Wang and Y. Cui, *Nano Lett.*, 2012, **12**, 3315–3321.
8 H. Wu, G. Zheng, N. Liu, T. J. Carney, Y. Yang and Y. Cui, *Nano Lett.*, 2012, **12**, 904–909.
9 M. Sangare, G. J. Fodjouong and X. Huang, *Mendeleev Commun.*, 2013, **23**, 284–285.
10 J. H. Kim, C. M. Park, H. Kim, Y. J. Kim and H. J. Sohn, *J. Electroanal. Chem.*, 2011, **661**, 245–249.
11 Q. Si, K. Hanai, T. Ichikawa, M. B. Phillipps, A. Hirano, N. Imanishi, O. Yamamoto and Y. Takeda, *J. Power Sources*, 2011, **196**, 9774–9779.
12 W. Wu, Y. Liang, H. Ma, Y. Peng and H. Yang, *Electrochim. Acta*, 2016, **187**, 473–479.
13 J. H. Kim, H. J. Sohn, H. Kim, G. Jeong and W. Choi, *J. Power Sources*, 2007, **170**, 456–459.
14 C. H. Doh, C. W. Park, H. M. Shin, D. H. Kim, Y. D. Chung, S. I. Moon, B. S. Jin, H. S. Kim and A. Veluchamy, *J. Power Sources*, 2008, **179**, 367–370.
15 J. H. Yom, J. K. Lee and W. Y. Yoon, *J. Appl. Electrochem.*, 2015, **45**, 397–403.
16 M. K. Datta and P. N. Kumta, *J. Power Sources*, 2007, **165**, 368–378.
17 J. Wang, M. J. Zhou, G. Q. Tan, S. Chen, F. Wu, J. Lu and K. Aminec, *Nanoscale*, 2015, **7**, 8023–8034.
18 X. Y. Wang, Z. Y. Wen, Y. Liu, Y. Huang and T. L. Wen, *Solid State Ionics*, 2011, **192**, 330–334.
19 X. J. Feng, J. Yang, Q. W. Lu, J. L. Wang and Y. Nuli, *Phys. Chem. Chem. Phys.*, 2013, **15**, 14420–14426.
20 B. C. Yu, Y. Hwa, J. H. Kim and H. J. Sohn, *Electrochim. Acta*, 2014, **117**, 426–430.
21 L. Yang, H. Li, J. Liu, Z. Sun, S. Tang and M. Lei, *Sci. Rep.*, 2015, **5**, 10908–10916.
22 S. O. Kim and A. Manthiram, *J. Mater. Chem. A*, 2015, **3**, 2399–2406.
23 Y. Ren and M. Li, *J. Power Sources*, 2016, **306**, 459–466.
24 M. Li, Y. Zeng, Y. Ren, C. Zeng, J. Gu, X. Feng and H. He, *J. Power Sources*, 2015, **288**, 53–61.
25 G. Hollinger and F. J. Himpsel, *Appl. Phys. Lett.*, 1984, **44**, 93–95.
26 T. Yasaka, S. Uenaga, H. Yasutake, M. Takakura, S. Miyazaki and M. Hirose, *Mater. Res. Soc. Symp. Proc.*, 1992, **259**, 385–390.
27 X. Liu, K. Xie, C. Zheng, J. Wang and Z. Jing, *J. Power Sources*, 2012, **214**, 119–123.
28 L. Khriachtchev, S. Novikov and O. Kilpela, *J. Appl. Phys.*, 2000, **87**, 7805–7813.

29 D. Nesheva, C. Raptis, A. Perakis, I. Bineva, Z. Aneva, Z. Levi, S. Alexandrova and H. Hofmeister, *J. Appl. Phys.*, 2002, **92**, 4678–4683.
30 F. Han, Y. Bai, R. Liu, B. Yao, Y. Qi, N. Lun and J. Zhang, *Adv. Energy Mater.*, 2011, **1**, 798–801.
31 L. Qie, W. Chen, Z. Wang, Q. Shao, X. Li, L. Yuan, X. Hu, W. Zhang and Y. Huang, *Adv. Mater.*, 2012, **24**, 2047–2050.
32 B. Guo, Q. Liu, E. Chen, H. Zhu, L. Fang and J. Gong, *Nano Lett.*, 2010, **10**, 4975–4980.
33 J. Yang, Y. Takeda, N. Imanishi, C. Capiglia, J. Xie and O. Yamamoto, *Solid State Ionics*, 2002, **152–153**, 125–129.
34 M. Miyachi, H. Yamamoto and H. Kawai, *J. Electrochem. Soc.*, 2007, **154**, A370–A380.
35 H. Y. Lee and S. M. Lee, *Electrochem. Commun.*, 2004, **6**, 465–469.
36 H. Nara, T. Yokoshima, T. Momma and T. Osaka, *Energy Environ. Sci.*, 2012, **5**, 6500–6505.
37 M. Li, Y. Yu, J. Li, B. Chen, X. Wu, Y. Tian and P. Chen, *J. Mater. Chem. A*, 2015, **3**, 1476–1482.
38 Y. Yao, J. Zhang, L. Xue, T. Huang and A. Yu, *J. Power Sources*, 2011, **196**, 10240–10243.
39 H. Tao, X. Yang, L. Zhang and S. Ni, *Mater. Chem. Phys.*, 2014, **147**, 528–534.
40 J. Lia and J. R. Dahn, *J. Electrochem. Soc.*, 2007, **154**, A156–A161.
41 J. S. Gnanaraj, M. D. Levi, E. Levi, G. Salitra, D. Aurbach, J. E. Fischer and A. Claye, *J. Electrochem. Soc.*, 2001, **148**, A525–A536.
42 X. Chen, X. Li, F. Ding, W. Xu, J. Xiao, Y. Cao, P. Meduri, J. Liu, G. L. Graff and J. G. Zhang, *Nano Lett.*, 2012, **12**, 4124–4130.
43 H. Wu, G. Chan, J. W. Choi, I. Ryu, Y. Yao, M. T. McDowell, S. W. Lee, A. Jackson, Y. Yang, L. Hu and Y. Cui, *Nat. Nanotechnol.*, 2012, **7**, 310–315.
44 J. Guo, X. Chen and C. Wang, *J. Mater. Chem.*, 2010, **20**, 5035–5040.
45 J. Wang, H. Zhao, J. He, C. Wang and J. Wang, *J. Power Sources*, 2011, **196**, 4811–4815.
46 A. Veluchamy, C. H. Doh, D. H. Kim, J. H. Lee, D. J. Lee, K. H. Ha, H. M. Shin, B. S. Jin, H. S. Kim, S. I. Moon and C. W. Park, *J. Power Sources*, 2009, **188**, 574–577.
47 C. Gui, S. Hao, Y. Liu, J. Qu, C. Yang, Y. Yu, Q. Wang and Z. Yu, *J. Mater. Chem. A*, 2015, **3**, 16551–16559.
48 M. K. Kim, B. Y. Jang, J. S. Lee, J. S. Kim and S. Nahm, *J. Power Sources*, 2013, **244**, 115–121.
49 W. Wu, J. Shi, Y. Liang, F. Liu, Y. Peng and H. Yang, *Phys. Chem. Chem. Phys.*, 2015, **17**, 13451–13456.